Research Article | Open Access

Soft Science

Zheng *et al*. *Soft Sci.* **2026**, *6*, 68 **DOI:**10.20517/ss.2026.94

Piezochromic metal-organic framework films for interfacial pressure mapping

Lin Zheng[1,#], Jinhui Gu[1,#], Junshuai Chen[1], Jun-Zhe Dong[1], Jia-Sen Xie[1], Ying Yang[1], Mingwei Gu[1], Xingyu Ma[1], Mengxing Huang[1], Jin Ge[1,*], Mei Pan[1,2,*], Cheng-Yong Su[1,*]

Keywords:
Piezochromic, MOF, pressure sensing, pressure mapping, thin film

Citation: Zheng, L.; Gu, J.; Chen, J.; Dong, J. Z.; Xie, J. S.; Yang, Y.; Gu, M.; Ma, X.; Huang, M.; Ge, J.; Pan, M.; Su, C. Y. Piezochromic metal-organic framework films for interfacial pressure mapping. *Soft Sci.* **2026**, *6*, 68.
https://dx.doi.org/10.20517/ss.2026.94

Received: 30 Apr 2026
First Decision: 4 Jun 2026
Revised: 18 Jun 2026
Accepted: 2 Jul 2026
Published: 3 Aug 2026

Academic Editor:
Wei Gao
Copy Editor:
Shu-Yuan Duan
Production Editor:
Shu-Yuan Duan

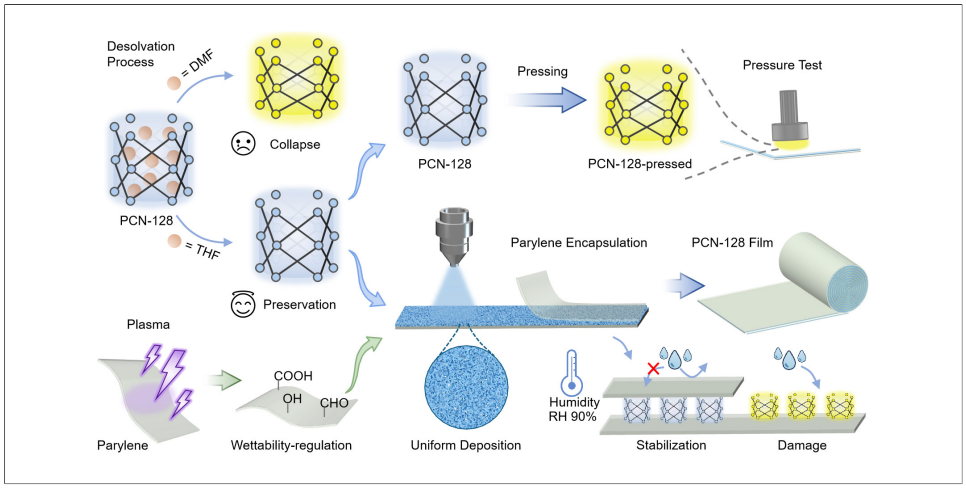

Abstract

Piezochromic metal-organic frameworks (MOFs) hold strong promise for interfacial pressure mapping owing to their structurally tunable sensitivity and sensing range. However, their practical deployment is hindered by structural instability during coating formation and under moisture exposure, as well as by the difficulty of obtaining color-uniform thin films. Herein, we report a solvent-exchange and encapsulation strategy that stabilizes MOF structures by weakening solvent-framework interactions and blocking moisture ingress, enabling highly stable piezochromic MOF films. Concurrently, highly color-uniform MOF films are realized through interfacial wettability regulation, enabling the identification of the surface roughness of 1000-grit sandpaper via pressure mapping. Moreover, the MOF coating process is adaptable to curved surfaces, allowing the recording of collision pressure distributions that are difficult to capture using electronic devices. This work demonstrates the great potential of piezochromic MOFs in film and coating formats for high-resolution interfacial pressure mapping.

[1]GBRCE for Functional Molecular Engineering, LIFM, IGCME, School of Chemistry, Sun Yat-Sen University, Guangzhou 510275, Guangdong, China.
[2]State Key Laboratory of Chemistry and Utilization of Carbon Based Energy Resources, College of Chemistry, Xinjiang University, Urumqi 830046, Xinjiang, China.
[#]These authors contributed equally to this work.

[*]**Correspondence to:** Prof. Cheng-Yong Su, Prof. Mei Pan, Prof. Jin Ge, GBRCE for Functional Molecular Engineering, LIFM, IGCME, School of Chemistry, Sun Yat-Sen University, Guangzhou 510006, Guangdong, China. E-mail: cesscy@mail.sysu.edu.cn; panm@mail.sysu.edu.cn; gejin@mail.sysu.edu.cn

INTRODUCTION

In precision manufacturing and advanced engineering systems, the spatial distribution of interfacial pressure critically governs structural reliability and service lifetime[1-7]. Consequently, a scalable and high-resolution approach for directly visualizing interfacial pressure is pivotal. Pressure-sensitive films provide an attractive approach because they can quantitatively detect both the magnitude and location of pressure[8-20]. Electrical pressure-sensitive films[21-25] often fail under localized pressure concentrations, where excessive loading damages embedded circuits. In contrast, piezochromic films[11,26-37] circumvent this limitation by transducing mechanical stimuli into color changes via intrinsic material responses, eliminating the need for a power supply and signal-reading circuits. Recently developed piezochromic materials[38-41] show great potential for this application; however, they are predominantly demonstrated in powder form rather than in freestanding and compact film form required for interfacial pressure detection. Therefore, their transformation into functional piezochromic films remains underexplored and represents a key gap requiring further investigation.

Among piezochromic materials, metal-organic frameworks (MOFs) are particularly attractive for interfacial pressure mapping due to their well-known structural diversity, which enables highly tunable sensing performance. However, the practical translation of these advantages into functional thin films is hindered by critical challenges associated with film formation. First, MOFs exhibit pronounced structural instability during coating processes[42], which disrupts their intrinsic framework integrity. Second, they are highly susceptible to moisture-induced degradation[43-45]. Third, achieving uniform films with homogeneous spatial MOF distribution remains difficult, resulting in inconsistent color responses across different areas of the films. Collectively, these issues severely limit the functionality of MOF-based piezochromic films and constrain their application in interfacial pressure mapping.

Here, we overcome the above limitations and realize highly stable and uniform piezochromic MOF films for interfacial pressure mapping. Using PCN-128[46] as a typical piezochromic MOF, we mitigate framework collapse by weakening solvent-framework interactions during film formation, while introducing encapsulation to block moisture ingress and preserve structural stability under ambient conditions. In parallel, highly uniform film formation is achieved through the control of interfacial wettability, which regulates droplet spreading behavior and promotes homogeneous spatial distribution of MOF crystals across large areas. This synergistic approach significantly improves color uniformity by fourfold, enabling precise pressure mapping that resolves the surface roughness of 1000-grit sandpaper. Moreover, the resulting coating process is adaptable to curved surfaces, allowing direct visualization of collision-induced pressure distributions that are difficult to capture using conventional electronic pressure sensing films. These results verify the strong potential of piezochromic MOFs for pressure sensing, and their performance in film and coating formats is expected to drive the development of new piezochromic MOFs and ultimately promote practical deployment.

EXPERIMENTAL

Materials and reagents

H_4ETTC was acquired from Bide Pharmatech Co., Ltd. $ZrCl_4$, $ZrOCl_2 8H_2O$, N,N-Dimethylformamide (DMF), tetrahydrofuran (THF), and Parylene C were obtained from Macklin Biochemical Co., Ltd. Trifluoroacetic acid was purchased from J&K Scientific Ltd. Formic acid was acquired from Guangzhou Chemical Reagent Factory. A commercial pressure-sensitive film (FUJ, MS) was obtained from FUJIFILM Corporation. The elastomer (3MTM VHBTM) was purchased from 3M. All reagents and solvents were used as received without further purification.

Characterization

Powder X-ray diffraction (PXRD) was performed using an automated multipurpose X-ray diffractometer (Bragg-Brentano geometry, Cu $K\alpha_1/\alpha_2$ radiation, λ = 1.54056/1.54433 Å, Rigaku Smartlab, Japan). Thermogravimetric analysis (TGA) was carried out on an analytical system (TG209, NETZSCH-Gerätebau GmbH, Germany) under nitrogen at atmospheric pressure and a heating rate of 10 °C min^{-1}. UV-vis absorption was recorded using an ultraviolet spectrophotometer (UV-2450, Shimadzu Corporation, Japan). Fluorescence spectra were obtained from a photoluminescence spectrometer (FLS980, Edinburgh Instruments Ltd., United Kingdom). Surface morphology was examined using a field-emission scanning electron microscope (FE-SEM, Hitachi SU8010, operated at 5 kV and 10 mA, Hitachi, Ltd., Japan). Optical images were captured using a stereo microscope (SOPTOP SZM7045, Sunny Optical Technology (Group) Company Limited, China). Parylene films were produced by parylene coating equipment [MQP-3001, Maggie Nano Technology (Suzhou) Co., Ltd, China]. Optical demonstration images of the film were captured using a camera (EOS 50D, Canon Inc., Japan). The pressure test was conducted using a tensile tester (EM2.502, Shenzhen Tesmart Instrument Equipment Co., Ltd., China). The water contact angle of the substrate was measured using a video-based optical contact angle system (OCA 50, DataPhysics Instruments GmbH, Germany). Nitrogen adsorption-desorption isotherms were collected using an automated high-throughput surface area and pore size analyzer [BSD-660M(A3M|B3M), Beishide Instrument Technology (Beijing) Co., Ltd., China]. The substrate surface was modified using a plasma cleaner (PT-6ST, Shenzhen Three and Wave of Electrical and Mechanical Technology Co., Ltd, China). A stylus profilometer (JS100A, Dongguan Jooin Technology Co., Ltd., China) was employed to measure the Parylene coating thickness. The sample was housed inside a constant climate chamber (BPS-50CL, Shanghai Yiheng Scientific Instruments Co., Ltd., China) under continuous monitoring. The sample was placed on a heating plate (JW-350BP, Wuhan Junwei Technology Co., Ltd., China) for thermal resistance assessment.

Preparation of the PCN-128 film

The preparation of PCN-128 films comprises two sequential steps: material synthesis and film fabrication.

Step I (synthesis of PCN-128): PCN-128 was synthesized following a reported protocol with slight modification[46]. In a typical synthesis, $ZrCl_4$ (300 mg), H_4ETTC (100 mg), trifluoroacetic acid (1.5 mL), and DMF (15 mL) were mixed in a reaction flask and heated to 120 °C under microwave irradiation for 1.5 h, followed by prolonged thermal treatment in an oil bath at the same temperature for 24 h. The as-synthesized crystals were isolated and thoroughly washed with DMF three times, followed by solvent exchange with THF through three additional washing cycles to ensure high purity. Subsequently, the THF solvent was refreshed daily for one week. Size-selective separation of PCN-128 crystals was achieved via differential centrifugation at 2000, 4000, 6000, 8000, and 9000 rpm for 3 min, respectively. The obtained crystals were then redispersed in THF to form a 20 mg mL^{-1} suspension for film fabrication.

Step II (spray-coating of PCN-128 films): In a typical experiment, a parylene layer (~ 1 μm) was deposited onto a cleaned glass substrate (5 × 5 cm^2) to serve as the supporting layer. The substrate was then treated by plasma (200 W, 2 min) to modify surface properties. Subsequently, the PCN-128 dispersion was spray-coated onto the substrate, and a conformal parylene overlayer (~ 100 nm) was finally deposited to encapsulate the film and enhance its environmental stability.

RESULTS AND DISCUSSION

Strategies for constructing uniform piezochromic MOF films.

In interfacial pressure mapping, a piezochromic film is placed between two contacting components, where the spatial distribution and magnitude of the applied pressure are encoded by the position and intensity of color changes [Figure 1A]. Central to this functionality is the piezochromic material, which must exhibit a

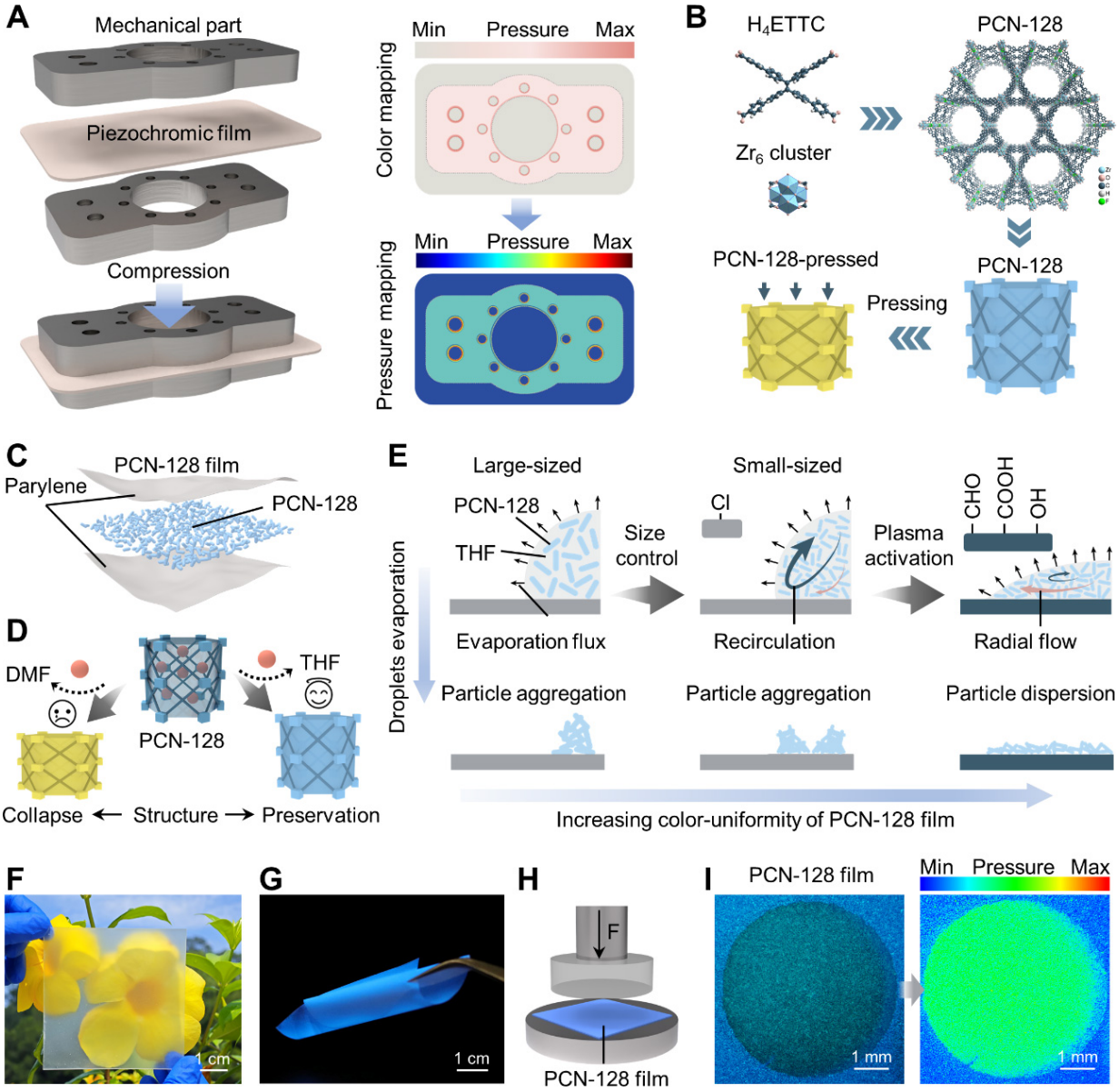

Figure 1. Application scenarios and piezochromic MOF film fabrication. (A) Schematic of interfacial pressure visualization using piezochromic films; (B) Crystal structure and piezochromic response of PCN-128; (C) Schematic illustration of the PCN-128 film architecture; (D) Solvent-regulation strategy for enhancing the structural stability of PCN-128; (E) Strategies for controlling the spatial uniformity of PCN-128 distribution on the substrate; (F) Images of PCN-128 film under ambient light; (G) Photoluminescence (PL) image of PCN-128 film under UV illumination; (H) Schematic of interfacial pressure detection test; (I) Interfacial pressure mapping using PCN-128 film (240 MPa). The elements in Figure 1F were photographed by the authors. DMF: Dimethylformamide; THF: tetrahydrofuran.

stable and irreversible color transition upon pressure. In this study, PCN-128[46], a Zr-based framework constructed from H_4ETTC linkers, is utilized as the active component. Under external pressure, conformational distortion of the H_4ETTC linkers induces framework collapse, resulting in a color transition from blue to yellow [Figure 1B and C].

Despite its piezochromic response, PCN-128 suffers from poor stability during film processing. During solvent evaporation, strong DMF (dimethylformamide)-framework interactions induce premature collapse, resulting in the loss of piezochromic response. To circumvent this issue, we exchanged the DMF with tetrahydrofuran (THF) to reduce such interactions and successfully preserved structural integrity during the desolvation process [Figure 1D].

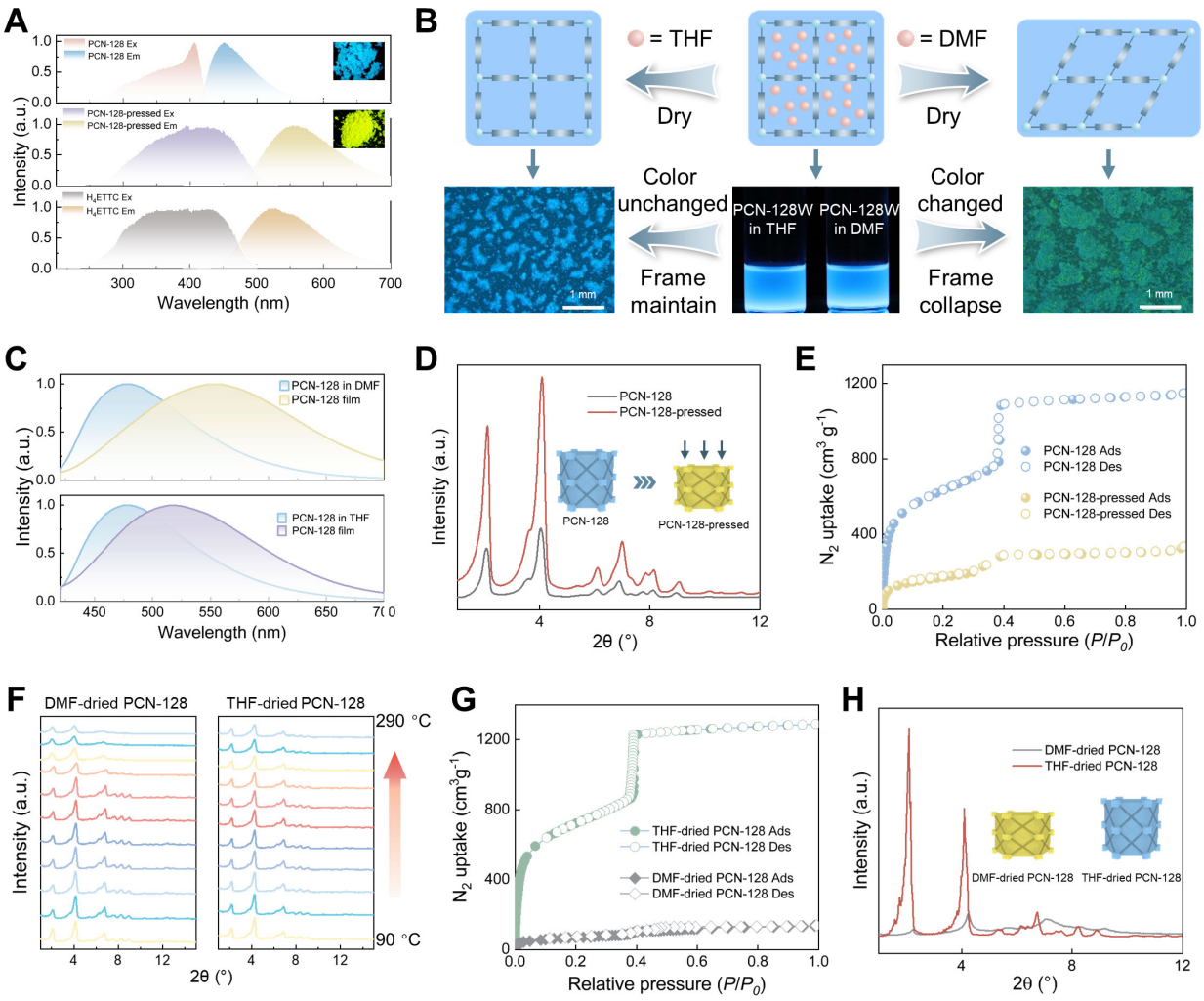

Figure 2. Mechanism of structural preservation via solvent exchange. (A) Fluorescence spectrum of PCN-128, PCN-128-pressed, and H_4ETTC; (B) Schematic diagram of solvent-framework interactions and images of PCN-128 (under UV); (C) Emission spectrum (excitation: 365 nm) of PCN-128 film drying from DMF and THF; (D) PXRD patterns of PCN-128 and PCN-128-pressed; (E) N_2 adsorption isotherms of PCN-128 and PCN-128-pressed measured at 77 K; (F) PXRD pattern of DMF-dried and THF-dried PCN-128 recorded from 90 to 290 °C; (G) N_2 adsorption isotherms of DMF-dried and THF-dried PCN-128; (H) PXRD patterns of DMF-dried and THF-dried PCN-128. DMF: Dimethylformamide; THF: tetrahydrofuran; PXRD: powder X-ray diffraction.

Besides preserving piezochromic behavior, the spatial distribution of MOF crystals is equally important, as it determines the homogeneity of the chromatic response. We improve the dispersion uniformity of PCN-128 by reducing particle size to enhance colloidal stability and by increasing substrate hydrophilicity to promote droplet spreading during drying, thereby minimizing aggregation domains [Figure 1E].

The optimized films exhibit excellent flexibility, appearing semi-transparent under ambient light, and emitting uniform blue fluorescence under ultraviolet (UV) light illumination [Figure 1F and G]. Upon compression, a distinct blue-to-yellow transition confirms pressure responsiveness [Figure 1H and I].

Effect of solvent-framework interaction on structural stability

The mechanism of solvent-removal-induced chromism in PCN-128 is similar to that induced by mechanical compression. As reported[46], PCN-128 undergoes a piezochromic transition from blue to yellow upon compression, accompanied by corresponding changes in UV-vis absorption and photoluminescence (PL) spectra [Figure 2A and Supplementary Figure 1]. In solution, PCN-128 exhibits blue emission in both DMF and THF [Figure 2B and C]. Upon solvent removal, the DMF-dried sample turns yellow-green, resembling the compressed state, whereas the THF-dried sample retains blue, indicating that the chromic response is governed by solvent-framework interactions.

To elucidate the structural origins of this behavior, both compressed and solvent-removed samples were analyzed. PCN-128-pressed retains overall crystallinity but exhibits subtle rearrangements, evidenced by peak shifts at low angles (< 4°) [Figure 2D]. Nitrogen adsorption measurements [Figure 2E] reveal a significant decrease in uptake from 1,090 $cm^3 \cdot g^{-1}$ (PCN-128) to 290 $cm^3 \cdot g^{-1}$ (PCN-128-pressed), indicating pore size reduction. A similar trend is observed for the DMF-dried PCN-128, which shows loss of low-angle PXRD peaks [Figure 2F] and a drastically reduced nitrogen uptake [Figure 2G], consistent with framework collapse. In contrast, the THF-dried PCN-128 retains both crystallinity and high porosity [Figure 2H]. These results indicate that stronger DMF-framework interactions induce structural collapse during solvent removal, whereas weaker THF interactions enable framework retention[47,48].

PCN-128 coating uniformity

PCN-128 films were fabricated via spray coating on parylene substrates, followed by encapsulation with parylene [Figure 3A and Supplementary Figure 2]. The areal fraction of crystals within the sprayed film, defined as the crystal coverage, serves as a key metric for evaluating the spatial distribution of MOF crystallites [Figure 3B]. This parameter is governed by both the particle size of PCN-128 and the surface wettability of the parylene substrate.

Particle size exerts a profound influence on the dispersion behavior in the precursor solution. PXRD patterns and SEM images confirm that downsizing PCN-128 from micrometer-scale wire-like crystals (length: 4.29 μm, diameter 384 nm) to nanorods (length: 866 nm, diameter 345 nm) does not alter its crystalline structure [Figure 3C and D and Supplementary Figure 3], and the material preserves its piezochromic response [Supplementary Figure 4]. The reduced particle size substantially enhances dispersion stability in THF, as evidenced by the absence of discernible sedimentation after 24 h [Figure 3E], and their photoluminescence in THF remains invariant even after 32 h [Figure 3F], underscoring excellent solvent stability. Moreover, the nanorods exhibit excellent dispersibility and stability in various solvents [Supplementary Figures 5 and 6]. A comparative study of films prepared from crystals of varying sizes reveals that smaller particles effectively mitigate aggregation, leading to a substantial increase in crystal coverage from 23% to 58% [Figure 3G and H].

The hydrophobic nature of the parylene substrate gives rise to a coffee-ring effect[49] during droplet drying, thereby compromising film uniformity. To address this issue, hydrophilic functional groups (-OH, -CHO, and -COOH) were introduced onto the parylene surface via oxygen plasma treatment[50], significantly enhancing wettability and lowering the water contact angle from 97.9° to 7.7° [Supplementary Figure 7]. The reduced contact angle alters the internal flow dynamics of the droplet, where outward radial flow dominates over internal recirculation[51,52], thereby facilitating uniform spreading of PCN-128 nanorods and improving film homogeneity [Figure 3I]. On pristine hydrophobic parylene substrates, pronounced coffee-ring-induced island-like aggregates are observed, with SEM images confirming severe nanorod agglomeration [Figure 3J]. Conversely, hydrophilic surface modification contributes to films that display uniform blue emission, while microscopic analysis reveals a well-dispersed nanorod network across the substrate [Figure 3K and Supplementary Figure 8].

Owing to the intrinsic photostability of PCN-128, the corresponding film exhibited negligible changes in both color and emission spectra after continuous UV irradiation for 7 days [Supplementary Figure 9], demonstrating its excellent optical stability. Moreover, the PCN-128 film demonstrated excellent thermal stability during the temperature cycling test between 50 and 150 °C [Supplementary Figure 10].

To further evaluate the mechanical robustness of the PCN-128 film, the PCN-128 film was attached onto a pre-stretched 3M tape, and different levels of compressive deformation were generated by gradually releasing the tape. The corresponding color and spectral variations of the PCN-128 film were systematically monitored

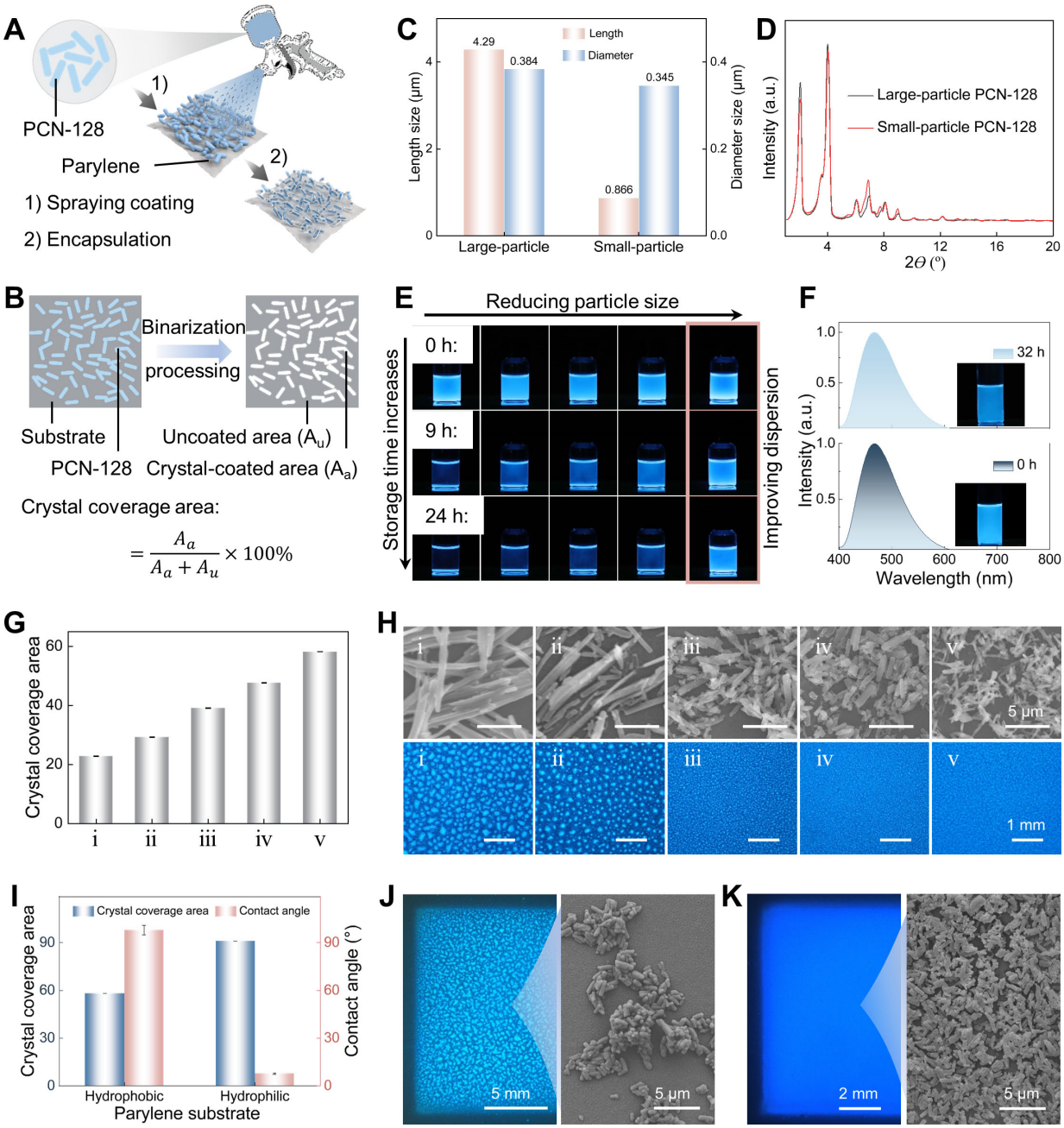

Figure 3. Formation of PCN-128 film coatings with high uniformity. (A) Schematic diagram of PCN-128 film preparation by spray coating; (B) Calculation process for crystals coverage area of PCN-128 film; (C) Particle size distribution histogram of large- and small-particle PCN-128; (D) PXRD patterns of large- and small-particle PCN-128. (E) Images of PCN-128 dispersions in THF with different particle sizes after standing for 24 h (under UV); (F) Emission spectrum (excitation: 365 nm) of a PCN-128 dispersion in THF before and after standing for 32 h. Crystal coverage data (G), SEM (Scale bars: 5 μm), and optical (Scale bars: 1 mm) images (under UV) (H) of PCN-128 films sprayed with crystals of various sizes; (I) Crystal coverage of PCN-128 films and substrate contact angles before and after surface modification of the parylene substrate. SEM and optical images (under UV) of PCN-128 films prepared using a parylene substrate with a hydrophobic (J) and hydrophilic (K) surface. Error bars indicate standard deviation (sample size n = 5). PXRD: Powder X-ray diffraction; THF: tetrahydrofuran; UV: ultraviolet; SEM: scanning electron microscope.

under different compression states. The results demonstrate that the PCN-128 film maintained excellent color uniformity even under 50% compression. Moreover, after 100 compression-release cycles, the film still exhibited stable optical performance [Supplementary Figure 11]. This outstanding mechanical stability can be attributed to the ultrathin parylene substrate (approximately 1 μm in thickness, Supplementary Figure 12), which provides the PCN-128 film with excellent flexibility. During compression, the flexible substrate

effectively dissipates external mechanical stress, allowing the color-responsive PCN-128 nanorods to maintain a relatively independent spatial distribution. Consequently, particle collision and aggregation-induced color variation are effectively suppressed, ensuring stable optical responses of the PCN-128 film during mechanical compression.

To enhance environmental stability, PCN-128 nanorod coatings were encapsulated with a 100 nm-thick parylene layer [Supplementary Figure 12]. The encapsulated films retain uniform luminescence after exposure to high humidity (RH = 90%) for 7 days, demonstrating the effectiveness of the barrier layer [Supplementary Figure 13]. Upon mechanical compression, the film exhibits a color change from blue to yellow [Supplementary Figure 14], attributed to the conformal encapsulation that suppresses moisture-induced degradation while preserving the intrinsic piezochromic response of PCN-128.

Collectively, these results highlight that synergistic control over particle size and substrate wettability, combined with encapsulation strategies, provides an effective pathway to fabricate uniform and environmentally robust MOF-based films. This approach is also expected to apply to other MOF-based films requiring high color uniformity [Supplementary Figure 15].

Pressure mapping resolution

The color uniformity of MOF-based film is primarily governed by two intertwined factors: the consistency of the emissive particle color and the uniformity of their distribution within the film [Figure 4A]. To quantitatively evaluate their contributions, we introduce a pixel-level image segmentation approach, in which chromatic distribution eigenvalues are employed as evaluation metrics to guide the optimization of fabrication processes for highly color-uniform films. In this approach, film images are segmented at the pixel level, and the corresponding color information is projected into the CIE Lab color space (CIE: International Commission on Illumination) to generate a three-dimensional chromaticity distribution profile. Films exhibiting color inhomogeneity or uneven particle distribution display broader and more scattered chromatic distributions, reflected by an increased volumetric spread in Lab space. To quantify this dispersion rigorously, the covariance matrix of the Lab coordinates is subjected to eigenvalue decomposition, and the average magnitude of the resulting eigenvectors is adopted as a metric for distribution compactness (Figure 4B, Supplementary Calculation method for film color uniformity evaluation). Accordingly, an MOF-based film with high color uniformity exhibits lower eigenvalues, whereas deviations in particle color or distribution lead to increased values, reflecting degraded color uniformity.

Using the film eigenvalues as a guiding metric, we first optimized the solvent used in the PCN-128 spray dispersion. Substituting DMF with THF results in eigenvalue reduction from 29.37 to 13.20 [Figure 4C], indicating 2.23-fold enhancement in color uniformity. This behavior can be rationalized by the strong interaction between DMF and the PCN-128 framework, which triggers structural collapse during solvent removal and results in crystal color variation. Consequently, films derived from DMF exhibit a heterogeneous distribution of yellow and blue crystallites, thereby deteriorating overall color uniformity. By contrast, THF, as a weaker interacting solvent, preserves the structural integrity of PCN-128, yielding uniformly blue emission within the film. Increasing the crystal loading further improves surface coverage and monotonically decreases the film eigenvalues [Figure 4D and Supplementary Figure 16], reflecting progressively enhanced uniformity. In addition, substrate surface chemistry also plays a decisive role. Upon hydrophilic modification of the parylene substrate, the film eigenvalues decrease sharply from 85 to 20, indicating 4.25-fold enhancement in uniformity [Figure 4E]. This improvement is attributed to the increased wettability of the substrate, which effectively suppresses the coffee-ring effect during solvent evaporation and facilitates a homogeneous distribution of PCN-128 crystals across the film.

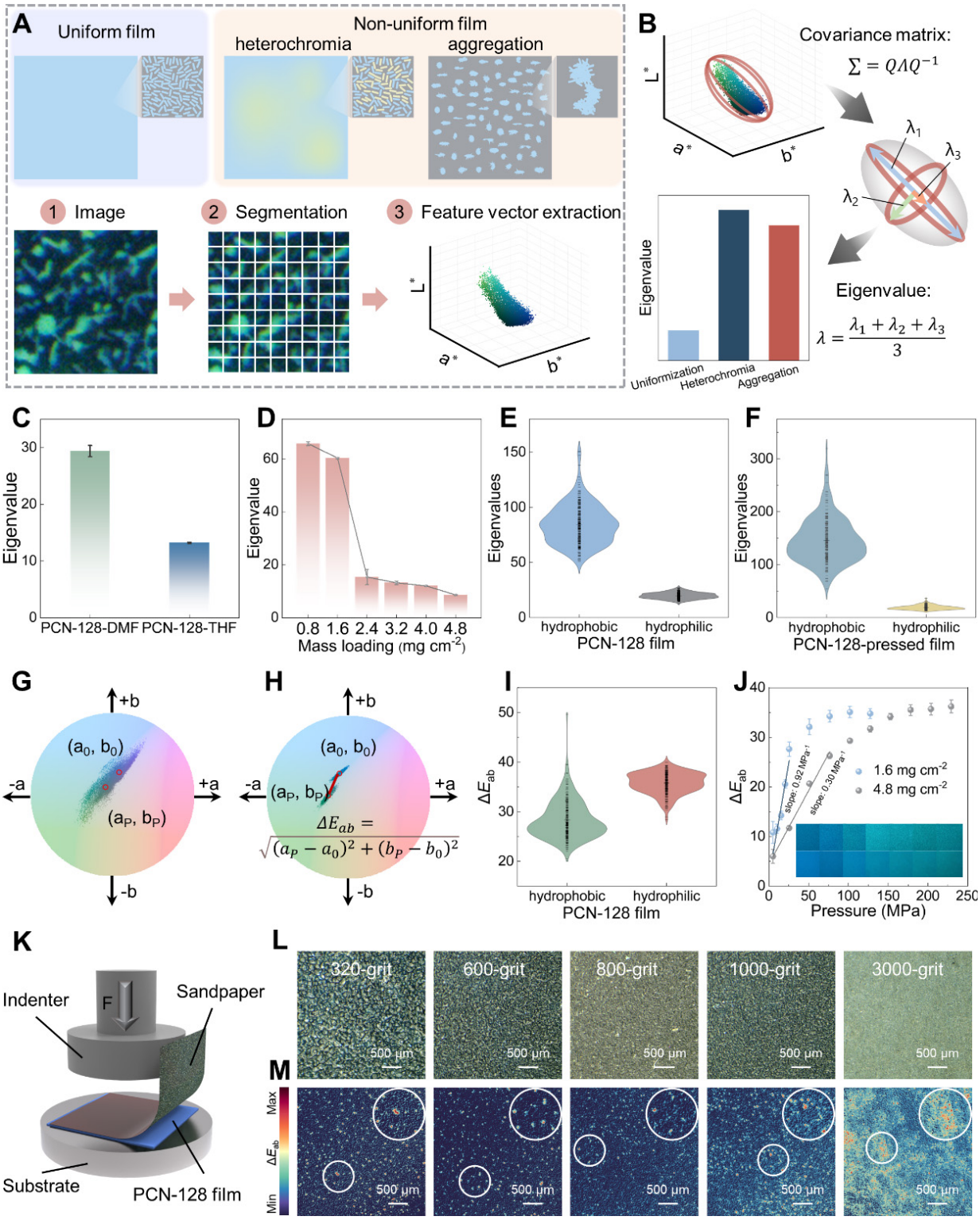

Figure 4. Evaluation of the pressure mapping resolution of PCN-128 films. (A) Image processing for film color uniformity assessment; (B) Algorithm for calculating film eigenvalues. Optimization of solvent (C), crystal loading (D), and substrate modification (E) based on film eigenvalues; (F) Comparison of film eigenvalues of PCN-128 film before and after substrate modification under compression. Calculation algorithm for the color difference (ΔE_{ab}) of PCN-128 film before (G) and after (H) substrate modification. (a_0, b_0) and (a_p, b_p) represent the average characteristic values of the PCN-128 film before and after compression; (I) ΔE_{ab} of PCN-128 film before and after substrate modification; (J) Color change of PCN-128 films versus pressure; (K) Schematic diagram of sandpaper indentation test. Different grits (320-, 600-, 800-, 1000-, and 3000-grit sandpaper) of sandpaper (L) and corresponding ΔE_{ab} images (M) of PCN-128 film (scale bar: 500 μm), and the illustration in the figure is a close-up. Error bars indicate standard deviation (sample size n = 5). DMF: Dimethylformamide; THF: tetrahydrofuran; ΔE_{ab}: the color difference of PCN-128 film before and after compression.

Enhanced color uniformity of the films leads to improved accuracy in pressure detection, as the sensing performance relies on the degree of chromatic contrast between the pre- and post-compression states. To eliminate interference from ambient lighting variations, the chromatic distributions are mapped onto the a-b plane of the Lab color space, and the color variation is quantified by calculating the Euclidean distance between the average feature values of the two states. In comparison to films containing aggregated crystals, those with homogeneously distributed crystallites display more localized and sharply bounded chromatic distributions in the a-b plane [Figure 4F-I and Supplementary Figure 17], enabling more reliable and precise evaluation of color difference (ΔE_{ab}) upon compression.

As the applied pressure increases, the ΔE_{ab} exhibits a linear response in the low-pressure regime, followed by a saturation behavior at higher pressure levels. The pressure-sensing range can be effectively tuned by regulating the surface loading of PCN-128 nanorods [Figure 4J, Supplementary Figure 18]. Specifically, the PCN-128 films with crystal loadings of 1.6 and 4.8 mg cm^{-2} exhibit pressure sensitivities of 0.92 and 0.30 MPa^{-1}, respectively, with corresponding sensing ranges of 5.09-101.86 MPa and 7.33-178.25 MPa. Both films reach signal saturation at 101.86 and 178.25 MPa, respectively, with minimum detectable pressures of 1.65 and 3.05 MPa. This phenomenon can be rationalized by considering that higher crystal coverage increases the number of pressure-responsive sites, thereby postponing saturation and broadening the measurable pressure range. The batch-to-batch reproducibility was verified using five independently prepared films, showing a standard deviation of 0.73 MPa in the response signals, which confirms the reliability and consistency of the fabrication process [Supplementary Figure 19].

Compared with representative piezochromic films reported in the literature [Supplementary Table 1], the PCN-128 film demonstrates a broader pressure sensing range while maintaining a competitive sensitivity. In addition, this work establishes an MOF-based piezochromic film platform and introduces a quantitative approach for evaluating color uniformity, addressing an important limitation in the characterization of piezochromic films. Furthermore, the developed fabrication strategy enables large-area preparation of MOF-based piezochromic films, highlighting its potential for scalable manufacturing and practical applications.

The combination of a tunable sensing range and high color uniformity endows the PCN-128 films with excellent spatial resolution for pressure detection. To substantiate this capability, imprinting experiments were conducted using sandpapers with varying grit sizes. The resulting patterns were analyzed via ΔE_{ab} distribution maps [Figure 4K]. With increasing grit number, the reduced surface roughness [Figure 4L] led to a higher density of contact points, as evidenced by the ΔE_{ab} distribution maps. Even for 1000-grit sandpaper, distinct spatial separation of contact points was preserved. However, upon further increasing the grit to 3000, the boundaries between neighboring contact regions gradually diminished, indicating a loss of spatial resolution [Figure 4M and Supplementary Figure 20].

Pressure mapping on planar and curved interfaces

PCN-128-based piezochromic films with high color uniformity hold significant promise for interfacial pressure sensing in assembled components, enabling precise mapping of spatial pressure distributions and thereby informing component design and manufacturing processes. Threaded fasteners represent essential sealing elements at pressure boundaries, where their engagement quality directly governs gas and liquid tightness. As the bolt is progressively tightened [Figure 5A], the film undergoes a color transition from blue to yellow at the contact interface. Continued tightening results in an expansion of the yellow region and an increase in ΔE_{ab}. The corresponding ΔE_{ab} maps indicate that both the extent and magnitude of interfacial pressure increase during tightening, while the pressure distribution remains spatially non-uniform [Figure 5B]. Cross-validation using a commercial Fuji film further confirms the interfacial stress distribution results [Supplementary Figure 21]. The ΔE_{ab} mapping of PCN-128 film and commercial Fuji film revealed a

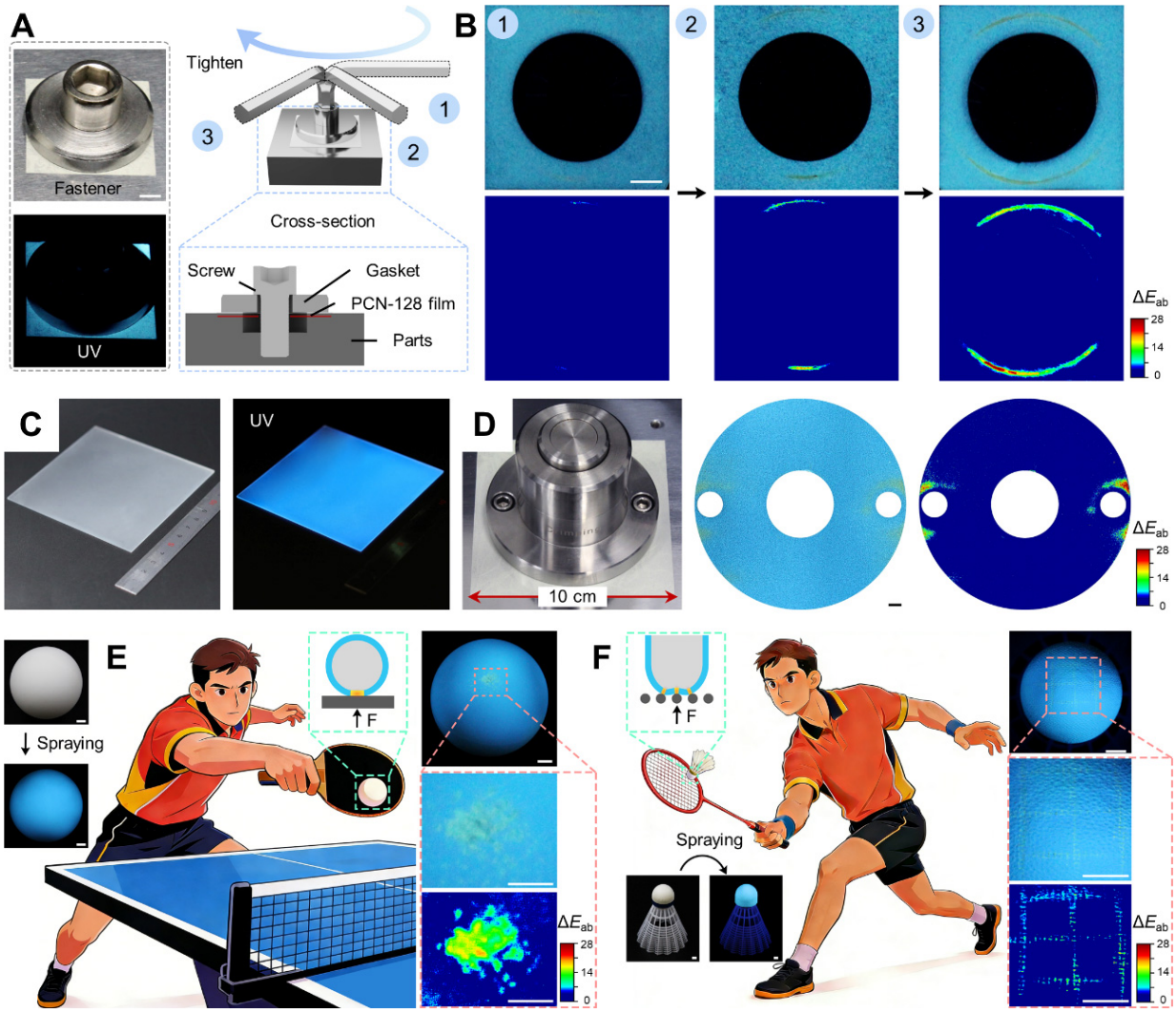

Figure 5. Demonstration of interfacial pressure mapping using PCN-128 films and coatings. (A) Schematic diagram illustrating the measurement of interface pressure in threaded fasteners using PCN-128 film (Scale bars: 1 cm); (B) PCN-128 film images (under UV) and ΔE_{ab} maps of the interface pressure testing process for threaded fasteners (Scale bars: 1 cm); (C) Large-area PCN-128 film (10 × 10 cm, under daylight and UV); (D) Interface pressure detection for the assembly of large-scale fasteners (Scale bars: 5 mm); (E and F) Detection of contact pressure on double-curved surfaces using sprayed PCN-128 film (Scale bars in E and F: 0.5 cm). UV: Ultraviolet; ΔE_{ab}: the color difference of PCN-128 film before and after compression.

pronounced non-uniform stress distribution at the fastening interface, suggesting insufficient sealing and the existence of potential leakage pathways. In addition, the PCN-128 film identifies a smaller effective contact area compared to the Fuji film, indicating its capability to accurately detect and resolve interfacial stress variations even under extremely small interfacial gaps.

Importantly, the scalability of the spray-coating process enables the fabrication of large-area films with preserved color uniformity [Figure 5C]. These films effectively identify pressure concentration regions during the assembly of large-scale fasteners, providing actionable insights for assembly optimization [Figure 5D and Supplementary Figure 22].

To further demonstrate the practical applicability of the PCN-128 film, we investigated the interfacial stress distribution between two flange joints during vacuum clamp tightening [Supplementary Figure 23]. Under ideal conditions, the clamp compresses the flanges symmetrically toward the center via its inclined surfaces,

while the enclosed O-ring undergoes elastic deformation under compression, thereby enabling a fully hermetic and leak-free seal. However, the PCN-128 film clearly reveals non-uniform contact stress distribution and localized incomplete interfacial contact between the flanges, indicating that an ideal sealing state is not achieved. These observations were further validated using a commercial Fuji film. However, its detection precision is inferior to that of the PCN-128 film.

In addition to scalable fabrication, spray coating offers superior conformability on complex curved surfaces. As proof of concept, PCN-128 nanorods were spray-coated onto spherical objects, including ping-pong and badminton balls, yielding homogeneous coatings [Figure 5E and F]. Upon mechanical impact, the films enable visualization of contact pressure distribution and magnitude on curved surfaces, highlighting their potential for probing interfacial mechanics in irregularly shaped components.

CONCLUSIONS

We demonstrate a simple yet scalable strategy for stabilizing and regulating piezochromic MOF films to enable high-resolution interfacial pressure mapping. The combination of solvent exchange, encapsulation, and interfacial wetting enhancement addresses two challenges in MOF film processing, meaning structural instability under coating formation and moisture exposure, and insufficient color uniformity. As a result, we achieve mechanically and optically stable MOF films with highly homogeneous color responses, enabling accurate pressure imaging and resolving fine surface features such as 1000-grit sandpaper. In addition, the coating process is readily extendable to curved and complex geometries, allowing pressure visualization in scenarios that are difficult to access using conventional electronic sensing platforms. These findings establish a practical pathway for translating piezochromic MOFs from crystalline materials into functional coating systems for advanced mechanical sensing applications.

DECLARATIONS

Authors' contributions

Conceptualization, supervision, project administration, writing-review and editing: Su, C. Y.; Pan, M.; Ge, J.
Methodology, formal analysis, investigation, data curation, visualization, and writing-original draft: Zheng, L.
Characterization and demonstration: Gu, J.
Assistance with the experiments and manuscript preparation: Dong, J. Z.; Chen, J.; Xie, J. S.; Yang, Y.; Gu, M.; Ma, X.; Huang, M.

Availability of data and materials

The data supporting the findings of this study are presented in this manuscript and Supplementary Materials.

AI and AI-assisted tools statement

A generative AI tool Doubao (Seedream 4.5, released 2025-11-28), a self-developed multimodal AI assistant by ByteDance, was used to assist in generating the human illustrations in Figure 5E and F. The AI-generated visual elements were reviewed and verified by the authors.

Financial support and sponsorship

This work was supported by the NKRD Program of China (2021YFA1500401), the National Natural Science Foundation of China (92461302, 22475242), and the Guangdong Basic and Applied Basic Research Foundation (2025A1515010271).

Conflicts of interest

All authors declared that there are no conflicts of interest.

Ethical approval and consent to participate

Not applicable.

Consent for publication

Not applicable.

Supplementary Materials

Supplementary Materials

REFERENCES

1. Bae, G.; Seo, M.; Lee, S.; Bae, D.; Lee, M. Colorimetric detection of mechanical deformation in metals using thin-film mechanochromic sensor. *Adv. Mater. Technol.* **2021**, *6*, 2100479. DOI
2. Cai, Y.; Chang, J.; Zhang, J.; et al. Dual-window broadband near-infrared mechanoluminescence in MgO-based phosphors. *Adv. Mater.* **2026**, *38*, e22739. DOI
3. Jin, X.; Li, L.; Zhao, S.; et al. Assessment of occlusal force and local gas release using degradable bacterial cellulose/$Ti_3C_2T_x$ MXene bioaerogel for oral healthcare. *ACS. Nano.* **2021**, *15*, 18385-93. DOI
4. Li, W.; Xiong, P.; Zheng, X.; et al. Micro-strain responsive near-infrared mechanoluminescence for potential nondestructive artificial joint stress imaging. *Adv. Mater.* **2025**, *38*, e05360. DOI
5. Lv, X.; Duan, T.; Huang, L.; et al. Robust solarblind ultraviolet mechanoluminescence in flexible elastomers without pre-irradiation. *Adv. Mater.* **2026**, *38*, e21006. DOI
6. Suo, H.; Li, L.; Sun, J.; et al. A self-powered tactile sensor resistant to environmental interference. *Adv. Mater.* **2025**, *38*, e16596. DOI
7. Yu, H.; Cao, W.; Han, W.; et al. A flexible self-powered occlusal force sensor array for assisting oral occlusion reconstruction. *Nano. Energy.* **2025**, *133*, 110466. DOI
8. Deng, Y.; Zhang, Y.; Bai, X.; et al. Photoluminescent-electrochromic synergy in passive devices for pressure visualization and multi-level encryption. *Adv. Funct. Mater.* **2025**, *36*, e12816. DOI
9. Smith, A. T.; Shen, K.; Hou, Z.; et al. Dual photo- and mechanochromisms of graphitic carbon nitride/polyvinyl alcohol film. *Adv. Funct. Mater.* **2021**, *32*, 2110285. DOI
10. Wang, X.; Zhang, H.; Yu, R.; et al. Dynamic pressure mapping of personalized handwriting by a flexible sensor matrix based on the mechanoluminescence process. *Adv. Mater.* **2015**, *27*, 2324-31. DOI
11. Zhang, H.; Chen, H.; Lee, J. H.; et al. Bioinspired chromotropic ionic skin with in-plane strain/temperature/pressure multimodal sensing and ultrahigh stimuli discriminability. *Adv. Funct. Mater.* **2022**, *32*, 2208362. DOI
12. Zhao, Y.; Peng, D.; Bai, G.; Huang, Y.; Xu, S.; Hao, J. Multiresponsive emissions in luminescent ions doped quaternary piezophotonic materials for mechanical-to-optical energy conversion and sensing applications. *Adv. Funct. Mater.* **2021**, *31*, 2010265. DOI
13. Hou, H. Y.; Zeng, X. Y.; Tang, J. X.; Li, Y. Q. Mechanical stability in flexible perovskite solar cells: Interface engineering and device design. *FlexMat* **2026**, flm2.70070. DOI
14. Li, X.; Wu, Z.; Chen, Z.; Shi, J. From touching to seeing: visualized pressure sensing in electronic skins. *Soft. Sci.* **2025**, *5*, 16. DOI
15. Lin, Z.; Wang, Y.; Nie, S.; et al. Island-bridge microstructured triboelectric pressure sensor for effective dynamic epidermal pulse monitoring. *Soft. Sci.* **2025**, *5*. DOI
16. Mao, Q.; Zhu, Z.; Meng, J.; Wang, T. Intelligent flexible memristors for artificial synapses and neuromorphic computing. *FlexMat* **2025**, *2*, 188-203. DOI
17. Munirathinam, K.; Li, L.; Shanmugasundaram, A.; Park, J.; Lee, D. Air-breakdown triboelectric nanogenerator inspired by transistor architecture for low-force human-machine interfaces. *Nano-Micro. Lett.* **2026**, *18*, 251. DOI
18. Wang, Z.; Zhao, Z.; Tu, Q.; et al. Graphene aerogel-based flexible pressure sensor for physiological signal detection and human-machine interaction. *Nano-Micro. Lett.* **2026**, *18*, 308. DOI
19. Wu, C.; Wang, S.; Wang, X.; et al. Programmable crack dynamics engineering enables flexible strain sensors with high linearity. *FlexMat* **2026**, flm2.70044. DOI
20. Xue, P.; Li, J.; Zhao, X.; et al. Full-photolithographic high-density skin-like transistor arrays for all-organic active-matrix displays. *Nano-Micro. Lett.* **2026**, *18*, 270. DOI PubMed PMC
21. Jang, J.; Ji, S.; Grandhi, G. K.; Cho, H. B.; Im, W. B.; Park, J. U. Multimodal digital X-ray scanners with synchronous mapping of tactile pressure distributions using perovskites. *Adv. Mater.* **2021**, *33*, 2008539. DOI PubMed PMC
22. Kaltenbrunner, M.; Sekitani, T.; Reeder, J.; et al. An ultra-lightweight design for imperceptible plastic electronics. *Nature* **2013**, *499*, 458-63. DOI

23. Kim, K. K.; Ha, I.; Won, P.; Seo, D.; Cho, K.; Ko, S. H. Transparent wearable three-dimensional touch by self-generated multiscale structure. *Nat. Commun.* **2019**, *10*, 2582. DOI PubMed PMC
24. Takei, K.; Takahashi, T.; Ho, J. C.; et al. Nanowire active-matrix circuitry for low-voltage macroscale artificial skin. *Nat. Mater.* **2010**, *9*, 821-6. DOI
25. Wang, C.; Hwang, D.; Yu, Z.; et al. User-interactive electronic skin for instantaneous pressure visualization. *Nat. Mater.* **2013**, *12*, 899-904. DOI
26. Cho, Y.; Oh, C. Y.; Son, E. J.; Kim, Y. S.; Shim, T. S. Biaxial mechanochromic behaviors of mechanically heterogeneous colloidal photonic crystal weave. *Adv. Opt. Mater.* **2024**, *12*, 2400135. DOI
27. Giese, M.; Blusch, L. K.; Khan, M. K.; Hamad, W. Y.; Maclachlan, M. J. Responsive mesoporous photonic cellulose films by supramolecular cotemplating. *Angew. Chem. Int. Ed.* **2014**, *53*, 8880-4. DOI
28. Guan, Y.; Li, H.; Zhang, S.; Niu, W. Mechanochromic photonic vitrimer thermal management device based on dynamic covalent bond. *Adv. Funct. Mater.* **2023**, *33*, 2215055. DOI
29. Yang, H.; Tu, D.; Wei, Y.; et al. Ultrasensitive mechanoluminescence of Pr^{3+}-doped perovskite oxide for 3D strain sensing and visualization. *Adv. Mater.* **2025**, *37*, e10747. DOI
30. Yang, W.; Yamamoto, S.; Sueyoshi, K.; Inadomi, T.; Kato, R.; Miyamoto, N. Perovskite nanosheet hydrogels with mechanochromic structural color. *Angew. Chem. Int. Ed.* **2021**, *60*, 8466-71. DOI
31. Yu, S.; Ma, D.; Qi, C.; Yang, D.; Huang, S. All-inone photonic crystals with multi-stimuli-chromic, color-recordable, self-healable, and adhesive functions. *Adv. Funct. Mater.* **2024**, *34*, 2411670. DOI
32. Zhang, P.; Shi, X.; Schenning, A. P. H. J.; Zhou, G.; De Haan, L. T. A Patterned mechanochromic photonic polymer for reversible image reveal. *Adv. Mater. Inter.* **2019**, *7*, 1901878. DOI
33. Zhang, S.; Sun, C.; Zhang, J.; et al. Reversible information storage based on rhodamine derivative in mechanochromic cholesteric liquid crystalline elastomer. *Adv. Funct. Mater.* **2023**, *33*, 2305364. DOI
34. Jia, C.; Xia, Y.; Zhu, Y.; Wu, M.; Zhu, S.; Wang, X. High-brightness, high-resolution, and flexible triboelectrification-induced electroluminescence skin for real-time imaging and human-machine information interaction. *Adv. Funct. Mater.* **2022**, *32*, 2201292. DOI
35. Qin, S.; Wei, W.; Tian, B.; et al. Self-recoverable, highly repeatable, and thermally stable mechanoluminescence for dual-mode information storage and photonic skin applications. *Adv. Funct. Mater.* **2024**, *34*, 2401535. DOI
36. Yang, H.; Wei, Y.; Ju, H.; et al. Microstrain-stimulated elastic-mechanoluminescence with dual-mode stress sensing. *Adv. Mater.* **2024**, *36*, 2401296. DOI
37. Zhang, K.; Chang, S.; Shang, Y.; et al. Mechanoluminescent/electric dual-mode sensors enabled by trace carbon nanotubes. *Small* **2024**, *20*, 2406398. DOI
38. Kiebala, D. J.; Style, R.; Vanhecke, D.; Calvino, C.; Weder, C.; Schrettl, S. Sub-micrometer mechanochromic inclusions enable strain sensing in polymers. *Adv. Funct. Mater.* **2023**, *33*, 2304938. DOI
39. Mo, S.; Meng, Q.; Wan, S.; et al. Tunable mechanoresponsive self-assembly of an amide-linked dyad with dual sensitivity of photochromism and mechanochromism. *Adv. Funct. Mater.* **2017**, *27*, 1701210. DOI
40. Qian, H.; Purwanto, N. S.; Ivanoff, D. G.; Halmes, A. J.; Sottos, N. R.; Moore, J. S. Fast, reversible mechanochromism of regioisomeric oxazine mechanophores: developing in situ responsive force probes for polymeric materials. *Chem* **2021**, *7*, 1080-91. DOI
41. Sun, D.; Wu, Y.; Han, X.; Liu, S. The host-guest inclusion driven by host-stabilized charge transfer for construction of sequentially red-shifted mechanochromic system. *Nat. Commun.* **2023**, *14*, 4190. DOI
42. Feng, L.; Wang, K.; Day, G. S.; Ryder, M. R.; Zhou, H. Destruction of metal-organic frameworks: positive and negative aspects of stability and lability. *Chem. Rev.* **2020**, *120*, 13087-133. DOI
43. Lu, Z.; Lin, H.; Jiang, Y.; et al. Confining the node accessibility of Zr-MOFs along one-dimensional channels toward high water-vapor cycle-stability. *Angew. Chem. Int. Ed.* **2025**, *64*, e202512722. DOI
44. Mchugh, L. N.; Mcpherson, M. J.; Mccormick, L. J.; et al. Hydrolytic stability in hemilabile metal-organic frameworks. *Nature. Chem.* **2018**, *10*, 1096-102. DOI
45. Zhang, L.; Wang, X.; Wang, X.; et al. Fabrication of a large-area flexible scintillating membrane for high-resolution X-ray imaging using an AIEgen-functionalized metal-organic framework. *Inorg. Chem.* **2023**, *62*, 6421-7. DOI
46. Zhang, Q.; Su, J.; Feng, D.; Wei, Z.; Zou, X.; Zhou, H. Piezofluorochromic metal-organic framework: a microscissor lift. *J. Am. Chem. Soc.* **2015**, *137*, 10064-7. DOI
47. Carrington, E. J.; Dodsworth, S. F.; Van Meurs, S.; Warren, M. R.; Brammer, L. Post-synthetic modification unlocks a 2D-to-3D switch in MOF breathing response: a single-crystal-diffraction mapping study. *Angew. Chem. Int. Ed.* **2021**, *60*, 17920-4. DOI
48. Carrington, E. J.; Mcanally, C. A.; Fletcher, A. J.; Thompson, S. P.; Warren, M.; Brammer, L. Solvent-switchable continuous-breathing behaviour in a diamondoid metal-organic framework and its influence on CO_2 versus CH_4 selectivity. *Nature. Chem.* **2017**, *9*, 882-9. DOI
49. Poulichet, V.; Morel, M.; Rudiuk, S.; Baigl, D. Liquid-liquid coffee-ring effect. *J. Colloid. Interface. Sci.* **2020**, *573*, 370-5. DOI

50. Golda-Cepa, M.; Brzychczy-Wloch, M.; Engvall, K.; Aminlashgari, N.; Hakkarainen, M.; Kotarba, A. Microbiological investigations of oxygen plasma treated parylene C surfaces for metal implant coating. *Mater. Sci. Eng. C.* **2015**, *52*, 273-81. DOI
51. Jeong, H.; Han, C.; Cho, S.; Gianchandani, Y.; Park, J. Analysis of extracellular vesicles using coffee ring. *ACS. Appl. Mater. Interfaces.* **2018**, *10*, 22877-82. DOI
52. Saxena, N.; Naik, T.; Paria, S. Organization of SiO_2 and TiO_2 nanoparticles into fractal patterns on glass surface for the generation of superhydrophilicity. *J. Phys. Chem. C.* **2017**, *121*, 2428-36. DOI